Numerical Investigation of Separated Transonic Turbulent Flows With a Multiple-Time-Scale Turbulence Model

S.-W. Kim
Institute for Computational Mechanics in Propulsion
Lewis Research Center
Cleveland, Ohio

January 1990

NASA

ICOMP
NASA
LEWIS RESEARCH CENTER
CASE WESTERN
RESERVE UNIVERSITY
INSTITUTE FOR COMPUTATIONAL MECHANICS IN PROPULSION

NUMERICAL INVESTIGATION OF SEPARATED TRANSONIC TURBULENT FLOWS
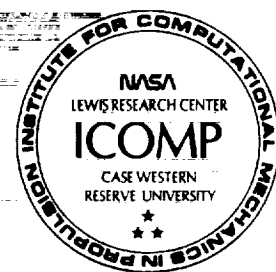
WITH A MULTIPLE-TIME-SCALE TURBULENCE MODEL

S.-W. Kim*
Institute for Computational Mechanics in Propulsion
Lewis Research Center
Cleveland, Ohio 44135

SUMMARY

Numerical investigation of transonic turbulent flows separated by streamline curvature and shock wave - boundary layer interaction is presented. The free stream Mach numbers considered are 0.4, 0.5, 0.6, 0.7, 0.8, 0.825, 0.85, 0.875, 0.90, and 0.925. In the numerical method, the conservation of mass equation is replaced by a pressure correction equation for compressible flows and thus incremental pressure is solved for instead of density. The turbulence is described by a multiple-time-scale turbulence model supplemented with a near-wall turbulence model. The present numerical results show that there exists a reversed flow region at all free stream Mach numbers considered whereas various k-ε turbulence models fail to predict such a reversed flow region at low free stream Mach numbers. The numerical results also show that the size of the reversed flow region grows extensively due to the shock wave - turbulent boundary layer interaction as the free stream Mach number is increased. These numerical results show that the turbulence model can resolve the turbulence field subjected to extra strains caused by the streamline curvature and the shock wave - turbulent boundary layer interaction and that the numerical method yields a significantly accurate solution for the complex compressible turbulent flow.

NOMENCLATURE

A_u	coefficient for axial velocity correction equation
A_v	coefficient for radial velocity correction equation
c	chord length of axisymmetric bump
$c_{p\ell}$	turbulence model constants for ϵ_p equation ($\ell=1,3$)
$c_{t\ell}$	turbulence model constants for ϵ_t equation ($\ell=1,3$)
$c_{\mu f}$	constant coefficient ($=0.09$)
f_μ	wall damping function for eddy viscosity equation
f_ϵ	wall damping function for ϵ_w equation
k	turbulent kinetic energy ($k=k_p + k_t$)
k_p	turbulent kinetic energy of eddies in production range
k_t	turbulent kinetic energy of eddies in dissipation range
k_e	effective thermal conductivity ($=k_m+ C_p\mu_t/\sigma_T$)
k_m	molecular thermal conductivity
M_∞	free stream Mach number
U_∞	free stream velocity
p	static pressure
P_t	stagnation pressure
P_r	production rate of turbulent kinetic energy
R	gas constant
R_e	Reynolds number
R_t	turbulent Reynolds number ($=k^2/(\nu\epsilon_1)$)
T	temperature
(u,v)	time averaged velocities in (x,r) coordinates
u_τ	friction velocity ($=\sqrt{(\tau_w/\rho)}$)
$u'v'$	Reynolds stress
V	velocity vector ($=\{u,v\}$)

(x,r)	axial and radial coordinates
y	radial distance from the wall
y^+	wall coordinate ($=u_\tau y/\nu$)
ϵ_p	energy transfer rate of turbulent kinetic energy
ϵ_t	dissipation rate of turbulent kinetic energy
ϵ_l	dissipation rate of turbulent kinetic energy
ϵ_w	dissipation rate inside the near-wall layer
κ	von Karman constant ($=0.41$)
μ	molecular viscosity
μ_e	effective viscosity ($=\mu+\mu_t$)
μ_t	turbulent viscosity
ν	kinematic viscosity of fluid
ν_t	turbulent eddy viscosity
ρ	density
σ_{kp}	turbulent Prandtl number for k_p equation
σ_{kt}	turbulent Prandtl number for k_t equations
σ_T	turbulent Prandtl number for energy equation
$\sigma_{\epsilon p}$	turbulent Prandtl number for ϵ_p equation
$\sigma_{\epsilon t}$	turbulent Prandtl number for ϵ_t equation
τ_w	wall shearing stress
Φ	dissipation function for energy equation

Superscripts

*	current value
'	incremental (or corrective) value

Mathematical symbol

$\sum$	summation

INTRODUCTION

The transonic flow over an axisymmetric curved hill [1] has received considerable attention in recent years as a bench mark test case to assess the capability of numerical methods as well as turbulence models to be used as design/analysis tools for fluid machinery. The transonic flow is schematically shown in Fig. 1. The boundary layer flow approaching the curved hill is subjected to an extra mean flow strain rate generated by the streamline curvature. The development of the viscous force on the wall depends on the extra mean flow strain rate. As the fluid particle travels along the wall, the mean momentum is dissipated by the strong viscous force and the flow eventually separates. As the free stream Mach number is further increased, a supersonic pocket is formed in the top region of the curved hill. As the strength of the shock wave is increased with the increasing free stream Mach number, the reversed flow region grows extensively due to the shock wave - boundary layer interaction. In numerical calculations of the transonic flow, correct prediction of the flow depends on the capability of a numerical method to resolve the compressible flow field which includes a supersonic flow region and a low Mach number reversed flow region and the capability of a turbulence model to properly resolve the turbulence field subjected to extra strain rates caused by the streamline curvature and the shock wave -boundary layer interaction. In this paper, calculations of the transonic flow at various free stream Mach numbers are made using a newly developed numerical method [2] and a multiple-time-scale turbulence model (hereafter abbreviated as the M-S turbulence model) [3,4]. A number of turbulence models, ranging from algebraic turbulence models to two-equation turbulence models incorporating a streamline curvature correction method, have been tested

4

and/or proposed in [5-7]. Varying degrees of success have been reported in these references. The present numerical results are compared with these numerical results as well as the measured data.

The Navier-Stokes equation solvers based on the pressure correction methods, also known as SIMPLE algorithms [8,9], are mostly used to solve incompressible flows the domain of which can be discretized by an orthogonal mesh. Due to their strongly convergent nature, pressure correction methods have been used extensively to solve complex turbulent flows including chemically reacting turbulent flows. In the numerical method used herein, the pressure correction method has been extended to solve incompressible as well as compressible flows with arbitrary, complex geometries. The compressible flow equations are mostly solved by approximate factorization methods and flux splitting methods. The Beam-Warming method [10] and the MacCormack method [11] are representatives of the approximate factorization methods and the Steiger-Warming method [12] is a representative of the flux-splitting methods. These methods were originally developed to solve the Euler equations and were then extended to include the viscous term to solve the Navier-Stokes equations. A few differences exist between the two classes of methods. In the latter class of methods, the density is solved for as a primary variable and the pressure is obtained from the equation state. For incompressible flows, the pressure no longer depends on the density and hence the latter class of methods fails for incompressible flows. These methods can also be extended to solve incompressible flows by including an artificial compressibility into the governing flow equations [13]. On the other hand, in the pressure correction methods, the incremental pressure is solved for as a primary variable, hence the method is valid for both incompressible and

5

compressible flows. Another difference between the two classes of methods can be found in the way the second order diffusion term is treated. In the pressure correction methods, the diffusion term is incorporated into the stiffness matrix while, in the other class of methods, the diffusion term is incorporated into the system of equations as the load vector term. For turbulent flows with extensive recirculation zones, the pressure correction methods may be numerically more stable than the other class of methods, conceptually; however, the pressure correction methods have mostly been used for incompressible flows and the approximate factorization methods and the flux splitting methods have mostly been used for compressible flows. Therefore, definitive advantages and disadvantages of these two classes of methods can not be discussed with confidence as yet.

A few papers to extend the SIMPLE method to solve compressible flows with complex geometries have appeared in recent years [14-16]. Some difficulties have been encountered in the course of these studies. One difficulty was identifying a suitable grid layout to solve the Navier-Stokes equations defined on complex geometries. In [14], a collocated grid layout was used and an artificial dissipation was included to prevent velocity-pressure decoupling. In the present numerical method and in [16], the velocities are located at the same grid points and the pressure is located at the centroid of pressure control volume formed by the four adjacent velocity grid points. This grid layout may yield a velocity-pressure decoupled solution if used together with the standard pressure correction procedure [17]. The mechanism that leads to the velocity-pressure decoupled solution is heuristically shown in [18]. In [14], the velocity-pressure decoupling was eliminated by using a non-conforming control-volume for mass imbalance calculation. In this case,

an uncertainty caused by the use of a non-conforming domain for the mass imbalance calculation needs to be further investigated. In the present numerical method, the velocity-pressure decoupling is eliminated by treating the pressure correction equation as a standard partial differential equation rather than treating it as a constraint condition. Further details are discussed in the following section. Another difficulty was to find a simple, yet strongly convergent, pressure correction equation valid for both incompressible and compressible flows. The capability to solve compressible flows is achieved by including a convective pressure correction term into the disturbed conservation of mass equation in one form or another. However, the numerical procedures to solve each compressible form pressure correction equation differ significantly from each other. A multi-step pressure correction algorithm was used in [14], and the SIMPLE-R [8] and the SIMPLE-C [19] were used in [15] and [16], respectively. In these methods, the density was also corrected from the incremental pressure. In the present method, only the pressure and the velocity are corrected from the incremental pressure and the density is obtained from the equation of state. Thus the present method is simpler than the other methods, and the multi-step pressure correction algorithm [14] is more involved than the other methods considered herein. The accuracy and the convergence nature of the present numerical method has been tested by solving a number of example flows. The example flows considered in [2] include: a developing channel flow, a developing pipe flow, a two-dimensional laminar flow in a 90 degree bent channel, polar cavity flows, and a turbulent supersonic flow over a compression ramp. More calculations of various complex turbulent flows using the same numerical method can be found in [20-22]. It can be seen from these numerical results

7

that the present numerical method yields accurate computational results even when highly skewed, unequally spaced, curved grids are used.

It has long been known that the turbulent transport is related to the time scale of energy containing large eddies and the dissipation of turbulent kinetic energy is related to the time scale of fine scale eddies in the dissipation range [23]. In M-S turbulence models, the turbulent transport of mass and momentum is described using the time scale of the large eddies and the dissipation rate is described using the time scale of the fine-scale eddies. Due to the physically consistent nature of the M-S turbulence models, these turbulence models are expected to yield significantly improved computational results compared with the single-time-scale turbulence models. However, the first M-S turbulence model [24] did not quite come up to the expectations due to a few shortcomings in the closure model. These shortcomings and a few differences between the two M-S turbulence models are discussed in the following section for the record. On the other hand, the present M-S turbulence model yields significantly improved computational results than the single-time-scale turbulence models for a number of complex turbulent flows [3,20,21]. These complex turbulent flows include: a wall-jet, a wake-boundary layer interaction flow, a turbulent flow over a backward-facing step, a confined coaxial swirling jet, turbulent flows over a strongly curved surface, and reattaching shear layers in a divergent channel. Calculation of more complex turbulent flows are in progress.

In numerical calculations of turbulent flows, the near-wall turbulence is usually described using the wall functions [25], two- or multi-layer turbulence models [26,27], and low Reynolds number turbulence models [28]. In the present study, the near-wall turbulence is described by a "partially

8

low Reynolds number approach" [4]. In this near-wall turbulence model, only the turbulent kinetic energy equations are extended to include the near-wall low turbulence region and the energy transfer rate and the dissipation rate inside the near-wall layer are obtained from algebraic equations. The algebraic equations were obtained from a k-equation turbulence model [29]. The advantages of the present near-wall turbulence model over the low Reynolds number turbulence models can be described as follows. The turbulence length scale of boundary layer flows is strongly related to the normal distance from the wall. This characteristic of the wall bounded turbulent flows can be described quite naturally by empirical algebraic equations. The low Reynolds number turbulence models can also be used to describe the wall bounded turbulent flows; however, more grid points have to be used to resolve the steep dissipation rate in the near-wall region. More detailed discussion on the advantages and disadvantages of various near-wall turbulence models, the development of the present near-wall turbulence model, and its application to fully developed turbulent channel and pipe flows can be found in [4]. It is also shown in [4] that the near-wall turbulence model can resolve the over-shoot phenomena of the turbulent kinetic energy and the dissipation rate in the region very close to the wall. Incorporation of the near-wall turbulence model into a k-ϵ turbulence model and its application to complex turbulent flows such as a supersonic turbulent flow over a compression ramp and a transonic flow over an axisymmetric curved hill can be found in [2] and [22], respectively.

REYNOLDS AVERAGED NAVIER-STOKES EQUATIONS AND NUMERICAL METHOD

The compressible turbulent flow equations are given as;

9

$$\frac{\partial}{\partial x}(\rho u) + \frac{1}{r}\frac{\partial}{\partial r}(\rho r v) = 0. \tag{1}$$

$$\frac{\partial}{\partial x}(\rho u u) + \frac{1}{r}\frac{\partial}{\partial r}(\rho r v u) = \frac{\partial}{\partial x}(\tau_{xx}) + \frac{1}{r}\frac{\partial}{\partial r}(r\tau_{xr}) - \frac{\partial p}{\partial x} \tag{2}$$

$$\frac{\partial}{\partial x}(\rho u v) + \frac{1}{r}\frac{\partial}{\partial r}(\rho r v v) = \frac{\partial}{\partial x}(\tau_{rx}) + \frac{1}{r}\frac{\partial}{\partial r}(r\tau_{rr}) - \frac{\partial p}{\partial r} - \frac{\tau_{\theta\theta}}{r} \tag{3}$$

$$\frac{\partial}{\partial x}(\rho C_p u T) + \frac{1}{r}\frac{\partial}{\partial r}(\rho r C_p v T) = \frac{\partial}{\partial x}\left(k_e\frac{\partial T}{\partial x}\right) + \frac{1}{r}\frac{\partial}{\partial r}\left(r k_e\frac{\partial T}{\partial r}\right) + u\frac{\partial p}{\partial x}$$

$$+ v\frac{\partial p}{\partial r} + \mu_e\Phi \tag{4}$$

where

$$\tau_{xx} = 2\mu_e\frac{\partial u}{\partial x} - \frac{2\mu_e}{3}(\nabla\cdot\mathbf{V}),$$

$$\tau_{xr} = \tau_{rx} = \mu_e\left(\frac{\partial u}{\partial r} + \frac{\partial v}{\partial x}\right),$$

$$\tau_{rr} = 2\mu_e\frac{\partial v}{\partial r} - \frac{2\mu_e}{3}(\nabla\cdot\mathbf{V}),$$

$$\tau_{\phi\phi} = 2\mu_e\frac{v}{r} - \frac{2\mu_e}{3}(\nabla\cdot\mathbf{V}),$$

10

$$\Phi = \left\{ 2\left[\frac{\partial u}{\partial x}\right]^2 + 2\left[\frac{\partial v}{\partial r}\right]^2 + 2\left[\frac{v}{r}\right]^2 + \left[\frac{\partial u}{\partial r} + \frac{\partial v}{\partial x}\right]^2 \right\} - \frac{2}{3}(\nabla \cdot V)^2,$$

$$\nabla \cdot V = \frac{\partial u}{\partial x} + \frac{1}{r}\frac{\partial(rv)}{\partial r},$$

and the density is obtained from the perfect gas law given as $p = \rho RT$. A turbulent Prandtl number (σ_T) of 0.75 was used for the energy equation. The molecular viscosity and the thermal conductivity were obtained from Sutherland's laws given as [30];

$$\frac{\mu}{\mu_0} = \left[\frac{T}{T_0}\right]^{3/2}\left[\frac{T_0 + S}{T + S}\right] \qquad (5)$$

where $\mu_0 = 1.716 \times 10^{-5}$ Kg/m-sec, $T_0 = 273.1^\circ$ Kelvin, $S = 110.6^\circ$ Kelvin; and

$$\frac{k_m}{k_0} = \left[\frac{T}{T_0}\right]^{3/2}\left[\frac{T_0 + S}{T + S}\right] \qquad (6)$$

where $k_0 = 0.0264$ Kg/m-K, $T_0 = 273.1^\circ$ Kelvin, and $S = 194.4^\circ$ Kelvin. The specific heat was obtained from a curve-fitted 4-th order polynomial, see [31] for details.

The pressure correction equation valid for both incompressible and compressible flows is described below. As in the standard pressure correction method, the density, the velocity, and the pressure are decomposed as;

11

$$\rho = \rho^* + \rho' \tag{7}$$

$$u = u^* + u', \tag{8}$$

$$v = v^* + v', \tag{9}$$

$$p = p^* + p' \tag{10}$$

Substituting eqs. (7-9) into eq. (1) yields:

$$\nabla \cdot (\rho' \mathbf{V}^*) + \nabla \cdot (\rho^* \mathbf{V}') + \nabla \cdot (\rho' \mathbf{V}') = - \nabla \cdot (\rho^* \mathbf{V}^*) \tag{11}$$

The third term on the left hand side of eq. (11) is neglected for simplicity in any of the pressure correction algorithms discussed below. The incremental pressure is related to the incremental density and the incremental velocities as;

$$p' = \rho' RT \tag{12}$$

$$u' = - A_u \frac{\partial p'}{\partial x} \tag{13}$$

$$v' = - A_v \frac{\partial p'}{\partial y} \tag{14}$$

where eq. (12) is obtained from the equation of state and eqs. (13-14) are obtained from the discrete u- and v-momentum equations, respectively. Substituting eqs. (12-14) into (11) yields, after some rearrangement;

$$\frac{\partial}{\partial x}\left[\frac{u^*}{RT}p'\right] + \frac{1}{r}\frac{\partial}{\partial r}\left[r\frac{v^*}{RT}p'\right] - \frac{\partial}{\partial x}\left[\rho^* A_u \frac{\partial p'}{\partial x}\right] - \frac{1}{r}\frac{\partial}{\partial r}\left[r\rho^* A_v \frac{\partial p'}{\partial r}\right] = - \nabla \cdot (\rho^* \mathbf{V}^*) \tag{15}$$

In the present numerical method, all flow variables, except pressure, are located at the same grid points and the pressure is located at the centroid of the cell formed by the four neighboring grid points. A few remarks on the pressure correction algorithm are in order for clarity. In the more standard pressure correction algorithms, the discrete pressure correction equation is obtained by directly substituting the discrete form incremental pressure - incremental velocity relations, eqs. (13-14), into eq. (11). In this case, the discrete pressure correction equation for a pressure grid point is given as a nine-diagonal system of equations for rectangular grids. This pressure correction equation can yield a velocity-pressure decoupled solution as discussed in [17,18]. Also this pressure correction equation is not diagonally dominant. On the other hand, in the present method, the continuous form pressure correction equation, given as eq. (15), is solved for incremental pressure. In this case, the discrete pressure correction equation is given as a five-diagonal system of equations for rectangular grids. This discrete pressure correction equation is strongly diagonally dominant even for highly skewed grids. Even the slightest symptom of velocity-pressure decoupling is not observed with the present pressure correction algorithm.

The capability to solve compressible flows with shock waves is achieved by the convective incremental pressure terms, the first two terms in the left hand side of eq. (15). These two terms properly take into account the hyperbolic nature of supersonic flows, and enable the capture of shock waves. In low Mach number flows and in the near-wall boundary layers of supersonic flows, the variation of density mostly depends on the local temperature. However, the dependence of density on temperature

has been ignored in deriving the convective terms for simplicity, see eq. (12). Yet, the dependence of density on temperature is clearly resolved in the present numerical method, since the incremental pressure is driven only by the mass imbalance evaluated from the conservation of mass, the right hand side of eq. (15), and the density is obtained from the equation of state. In fact, it can be seen in [32] that low Mach number flows can be solved even without the convective incremental pressure terms. Equally importantly, use of the simplified incremental pressure -incremental density relationship still yields a rapidly convergent solution as shown in the following section. Also note that the present pressure correction algorithm is significantly simpler than the multi-step pressure correction algorithm [14].

In solving the system of equations, the power-law upwinding [8] is used for all convection-diffusion equations except for the pressure correction equation. The upwind differencing [8] is used for the pressure correction equation. In the region very close to the wall, highly fine grids need to be used to resolve the thin boundary layer properly. In this region, the numerical method is second order accurate; however, the method becomes first order accurate in the free stream region where the mesh is coarse. Each differential equation is solved sequentially until the relative error for each flow variable becomes smaller than the prescribed convergence criterion and the mass imbalance in eq. (15) becomes negligible. The incremental pressure is obtained by solving eq. (15). In solving the discrete system of equations, the off-diagonal terms may be moved to the load vector term and the resulting system of equations can be solved using a tri-diagonal matrix algorithm (TDMA). The corresponding incremental velocities are obtained from eqs. (13-14). The flow variables

are updated using eqs. (8-10), and these updated flow variables are used in computing the new current flow variables by solving eqs. (2-4) and the turbulence equations.

TURBULENCE EQUATIONS

The M-S turbulence model supplemented with the near-wall turbulence model is summarized below for completeness. The turbulent kinetic energy and the energy transfer rate equations for the energy containing large eddies are given as;

$$\frac{\partial}{\partial x}(\rho u k_p) + \frac{1}{r}\frac{\partial}{\partial r}(r\rho v k_p) - \frac{\partial}{\partial x}\{(\mu+\frac{\mu_t}{\sigma_{kp}})\frac{\partial k_p}{\partial x}\} - \frac{1}{r}\frac{\partial}{\partial r}\{r(\mu+\frac{\mu_t}{\sigma_{kp}})\frac{\partial k_p}{\partial r}\} = \rho Pr - \rho\epsilon_p \quad (16)$$

$$\frac{\partial}{\partial x}(\rho u \epsilon_p) + \frac{1}{r}\frac{\partial}{\partial r}(r\rho v \epsilon_p) - \frac{\partial}{\partial x}\{(\mu+\frac{\mu_t}{\sigma\epsilon_p})\frac{\partial \epsilon_p}{\partial x}\} - \frac{1}{r}\frac{\partial}{\partial r}\{r(\mu+\frac{\mu_t}{\sigma\epsilon_p})\frac{\partial \epsilon_p}{\partial r}\}$$

$$= \rho c_{p1}\frac{Pr^2}{k_p} + \rho c_{p2}\frac{Pr\epsilon_p}{k_p} - \rho c_{p3}\frac{\epsilon_p^2}{k_p} \quad (17)$$

where $Pr=\nu_t\Phi$ is the production rate. The turbulent kinetic energy equation and the dissipation rate equation for the fine scale eddies are given as:

$$\frac{\partial}{\partial x}(\rho u k_t) + \frac{1}{r}\frac{\partial}{\partial r}(r\rho v k_t) - \frac{\partial}{\partial x}\{(\mu+\frac{\mu_t}{\sigma_{kt}})\frac{\partial k_t}{\partial x}\} - \frac{1}{r}\frac{\partial}{\partial r}\{r(\mu+\frac{\mu_t}{\sigma_{kt}})\frac{\partial k_t}{\partial r}\} = \rho\epsilon_p - \rho\epsilon_t \quad (18)$$

$$\frac{\partial}{\partial x}(\rho u \epsilon_t) + \frac{1}{r}\frac{\partial}{\partial r}(r\rho v \epsilon_t) - \frac{\partial}{\partial x}\{(\mu+\frac{\mu_t}{\sigma\epsilon_t})\frac{\partial \epsilon_t}{\partial x}\} - \frac{1}{r}\frac{\partial}{\partial r}\{r(\mu+\frac{\mu_t}{\sigma\epsilon_t})\frac{\partial \epsilon_t}{\partial r}\}$$

$$= \rho c_{t1}\frac{\epsilon_p^2}{k_t} + \rho c_{t2}\frac{\epsilon_p\epsilon_t}{k_t} - \rho c_{t3}\frac{\epsilon_t^2}{k_t} \quad (19)$$

The eddy viscosity is given as;

$$\mu_t = \rho c_\mu f \frac{k^2}{\epsilon_p} \tag{20}$$

The turbulent kinetic energy equations, eqs. (16) and (18), are defined for the entire flow domain while the energy transfer rate equation, the dissipation rate equation and the eddy viscosity equation are valid for the flow domain away from the near-wall region. The turbulence model constants are given as; $\sigma_{kp}=0.75$, $\sigma_{kt}=0.75$, $\sigma_{\epsilon p}=1.15$, $\sigma_{\epsilon t}=1.15$, $c_{p1}=0.21$, $c_{p2}=1.24$, $c_{p3}=1.84$, $c_{t1}=0.29$, $c_{t2}=1.28$, and $c_{t3}=1.66$. Details on the present M-S turbulence model can be found in [3].

The energy transfer rate and the dissipation rate inside the near-wall layer are given as;

$$\epsilon_p = \epsilon_t = \frac{\epsilon_1}{f_\epsilon} \tag{21}$$

where

$$\left. \begin{aligned} \epsilon_1 &= \frac{c_\mu f^{3/4} k^{3/2}}{\kappa y} \\[2em] f_\epsilon &= 1 - \exp(-A_\epsilon R_t) \\[2em] R_t &= \frac{k^2}{\nu \epsilon_1} \\[2em] A_\epsilon &= \frac{c_\mu f^{3/2}}{2\kappa^2} \end{aligned} \right\} \tag{22}$$

and the eddy viscosity for the near-wall layer is given as;

$$\nu_t = c_{\mu f} \; f_\mu \; \frac{k^2}{\epsilon_1} \qquad\qquad (23)$$

where $f_\mu = 1 - 1./\exp(A_1 \sqrt{R_t} + A_2 R_t^2)$. The coefficients A_1 and A_2 are given as 0.025 and 0.00001, respectively, see [4].

The domain for each differential equation is shown schematically in Figure 2. For wall bounded turbulent flows, the equilibrium region extends from $y^+ \approx 30$ to $y^+ \approx 300$. Thus the partition between the near-wall region and the fully turbulent outer region can be located between y^+ greater than 30 and less than 300 approximately. Recall that the present near-wall turbulence model and the k-equation turbulence model [29] from which the present near-wall turbulence model is derived are valid for the entire flow domain of equilibrium boundary layer flows. Thus the computational results do not depend appreciably on the location of the partition. However, if the partition is located too far away from the wall (i.e., $y^+ > 1000$), then the numerical results in the near-wall region may become similar to those obtained using a k-equation turbulence model.

A few differences between the present M-S turbulence model and that of [24] are summarized in this paper for the record. Firstly, the eddy viscosity equation in [24] is given as;

$$\nu_t = c_{\mu f} \frac{k k_p}{\epsilon_p} \qquad\qquad (24)$$

Numerical calculations of complex turbulent flows showed that the ratio of k_t/k_p can vary significantly in regions where the turbulence is in a

17

strongly inequilibrium state. Eq. (24) implies that the small scale eddies contained in the dissipation range may not contribute significantly to the turbulent transport of mass and momentum. This anomaly can be cured if the partition between the large eddies and the small eddies is moved toward the very high wave number region so that the k_t may be negligibly small in all occasions. However, in this case, the multiple-time-scale turbulence model can be reduced to a single-time-scale turbulence model as discussed in [24]. Secondly, in the present M-S turbulence model, the variable energy transfer functions were obtained from a physical dimensional analysis [30]. On the other hand, the M-S turbulence model in [24] contains such a variable energy transfer function only in the energy transfer rate equation. Hence the load functions of the energy transfer rate equation and the dissipation rate equation lack symmetry. Thirdly, in the present M-S turbulence model, the model constants were obtained by solving a five by five system of equations obtained by transforming the M-S turbulence equations into asymptotic equations for the decay rate of grid turbulence [33] and the growth rate of turbulence intensity [34]. Lastly, of practical importance, the eddy viscosity equation given as eq. (24) is inconsistent with the near wall analysis unless k_t vanishes in the near-wall equilibrium region, see [3]. In application to complex turbulent flows, arbitrary ratios of k_t/k_p were used as a near wall boundary condition together with the standard wall functions [24,35]. A wall function for the M-S turbulence model obtained from a near-wall analysis is given in [3], if any wall function need to be used. Also an arbitrary ratio of k_t/k_p was used as an inlet boundary condition in a number of boundary layer calculations [35]. In this case, the calculated shear layer expands rapidly so that the turbulence field can adjust itself to the ill-posed inlet boundary

18

condition, see [3].

COMPUTATIONAL RESULTS

The measured data for the transonic flow over an axisymmetric curved hill at various free stream Mach numbers can be found in [1,5,36]. In the experiment, an axisymmetric circular-arc bump of thickness 1.9 cm and a chord length of 20.3 cm was attached 60 cm downstream of a circular cylinder with the external diameter of 15.2 cm. The numerical results for $M_\infty=0.875$ and $R_e=13.2\times10^6$/m are compared with the measured data presented in [36]. The boundary layer thickness of the approaching transonic flow was 0.01 meters for $M_\infty=0.875$. The other numerical results for the rest of the free stream Mach numbers at $R_e=10\times10^6$/m are compared with the measured data given in [5].

In the following calculations, the inlet boundary is located at one chord length upstream of the forward corner of the bump; and the exit boundary, at one chord length downstream of the rear end of the bump. Some degree of uncertainty that may be caused by numerical diffusion and inadequate grid size can always exist in any numerical analysis. To reduce the numerical uncertainty, three different meshes (78x53, 108x65, and 145x65 grid points in the axial and radial directions, respectively) have been used in the present study. The computational results obtained using the first two grids differed by no more than a few percent; and the latter two, by no more than one percent. The computational results presented herein were obtained using the finest grid shown in Figure 3. The inlet boundary condition for the axial velocity and the turbulent kinetic energy were obtained from experimental data for a fully developed flat plate flow [37]. The non-dimensional velocity and the turbulent kinetic energy

profiles were scaled to yield a boundary layer thickness of 0.01 meters at the inlet boundary. Uniform static pressure and uniform enthalpy were also prescribed at the inlet boundary. The no-slip boundary condition for velocities, a vanishing turbulent kinetic energy, and a constant temperature which corresponds to the free stream stagnation temperature were prescribed at the solid wall boundary. The free stream flow condition was prescribed at the top boundary, and a vanishing gradient boundary condition was used for all flow variables at the exit boundary. The partition between the near-wall layer and the external region was located at approximately one percent of the boundary layer thickness away from the wall. Thus the partition is located at $y^+ \approx 80$ (for $M_\infty = 0.875$) at the inlet boundary and 11 grid points were allocated inside the near-wall layer. The mesh size of the first grid point on the bottom wall was $\Delta y^+ \approx 1.25$ and the grid size in the normal to the wall direction was increased by a factor of approximately 1.15. The initial guess was obtained by extending the inlet boundary condition in the axial direction. An uncertainty that can be caused by the location of the inlet boundary and the inlet boundary conditions is clarified by comparing the numerical results with the measured data at $x/c = -0.25$.

The convergence history for $M_\infty = 0.875$ is shown in Figure 4. Each iteration consists of 7 sweeps of the pressure correction equation and 3 sweeps for the rest of the flow equations in the axial and in the radial directions, respectively. The pressure was updated using an under-relaxation factor of 0.57; and the rest of the flow variables, using an under-relaxation factor of 0.47. The relative error for each flow variable shown in Figure 4(a) is defined as;

$$R_i = \text{Max}\{|(a_{i,j}^{n+1} - a_{i,j}^{n})/A_i^{n+1}|, \ j=1,N\} \qquad (25)$$

where the superscript n denotes the iteration level; the subscript i={u,v,p,T} denotes each flow variable; the subscript j denotes each grid point; N denotes the total number of degrees of freedom for each flow variable; and A_i denotes the maximum magnitude of the i-th flow variable. The convergence histories for the other scalar variables (k_p, ϵ_p, k_t, and ϵ_t) are almost the same as that of temperature. The mass imbalance shown in Figure 4(b) is defined as;

$$R_2 = 1/N_c \ [\ \sum_{c=1}^{N_c} \{\nabla \cdot (\rho V)\}^2_c] \qquad (26)$$

where N_c is the total number of the pressure control volumes. The "practically" converged solution was obtained in approximately 1000 iterations for all the free stream Mach numbers considered. Note that, in control-volume based finite difference methods, the discrete system of equations is derived by integrating the governing differential equations over each control volume. For curvilinear grids, the required number of interpolations to obtain flow variables at the cell boundaries is significantly reduced by using the present grid layout than the one used in [18]. The strongly convergent nature of the present numerical method is partly attributed to the grid layout which required fewer interpolations and the pressure correction algorithm which yields a diagonally dominant system of equations even when highly skewed meshes are used. It can also be found in Figure 4(b) that the mass imbalance converges almost monotonically. Such a monotonically convergent nature is attributed to the use of the under-relaxation. With the use of these under-relaxation

21

parameters, divergence or convergence to an erroneous solution was not encountered.

The calculated iso-Mach lines are shown in Figure 5, where the incremental Mach number between the contour lines is constant for each free stream Mach number. It can be seen in this figure that a small supersonic pocket first appears at M_∞=0.80. The iso-Mach lines are almost symmetric at low free stream Mach numbers and the symmetry is lost as the size of the supersonic pocket grows with the increasing free stream Mach number. It can be seen from these figures that the present numerical method can cleanly resolve the transonic flows from the low to the high transonic free stream Mach number. The size of the supersonic pocket for M_∞=0.925 also compares favorably with that obtained using the MacCormack scheme [5]. The calculated shock is slightly more spread out than that of [5] since the present numerical method becomes first order accurate in the free stream region where coarse grids are used. However, the slightly smeared shock does not impair the numerical results appreciably as can be seen in this section.

The calculated static pressure distributions on the wall are compared with the measured data as well as the other numerical results in Figure 6. It can be seen in the figure that the pressure distributions on the wall obtained by the MacCormack scheme using the King-Johnson algebraic turbulence model [5] (hereafter abbreviated as K-J model) compare most favorably with the measured data. The present numerical results show that the calculated shocks are located somewhat downstream of the measured data for all free stream Mach numbers. This discrepancy is attributed to the turbulence model which slightly under-estimates the Reynolds stress. For M_∞=0.875, the present result compares more favorably with the measured data

than does the one obtained by the MacCormack scheme using the Wilcox-Rubesin Turbulence model (hereafter, abbreviated as W-R model) [7]. However, it can be found in [6] that the W-R model yields substantially improved numerical results for the wall pressure and the mean velocity if the free stream condition is prescribed at the outer boundary.

The streamline and the pressure contour lines for $M_\infty = 0.875$ are shown in Figures 7(a) and 7(b), respectively. These contour lines also indicate that the present numerical method can cleanly resolve the transonic turbulent flow.

The calculated separation and reattachment locations are compared with the measured data and the other numerical results in Figure 8. It is shown in this figure that the present method successfully predicts the existence of the reversed flow region at all free stream Mach numbers. At low free stream Mach numbers, the present results compare more favorably with the measured data than do those obtained by the MacCormack scheme using the K-J turbulence model [5]. As the free stream Mach number is increased, the present method slightly under-predicts the size of the reversed flow region compared with the measured data and the numerical results obtained using the K-J turbulence model. This under-prediction of the reversed flow region is a result of the calculated shocks located slightly downstream of the measured data. It is also shown in this figure that the Jones-Launder k-ϵ turbulence model [5] and a k-ϵ turbulence model supplemented with a streamline curvature correction method [6] fail to predict the reversed flow region at low free stream Mach numbers. These turbulence models also under-predict the reattachment locations at high free stream Mach numbers as shown in the figure.

The mean velocity profiles for $M_\infty = 0.875$ at five axial locations are

compared with the measured data as well as the other numerical results in Figure 9. At x/c=-0.25, the calculated mean velocity profile and the measured data compare favorably with each other, which indicates that the inlet boundary condition used in the present study is a good approximation to the experiment at the inlet boundary. It can be seen in the figure that all numerical results exhibit fair comparison with the measured data. In particular, the mean velocity profile obtained using the W-R turbulence model [7] compares less favorably with the measured data than the other numerical results. Again, it can be found in [6] that the W-R model yields an improved mean velocity profile if the free stream condition is prescribed at the outer boundary. It is also shown in the figure that a k-ϵ turbulence model incorporating an improved wall function [25] under-predicts the magnitude of mean velocity at x/c=0.75 and 0.875 [39]. This under-prediction in the mean velocity is caused by the over-predicted Reynolds stress at the same axial locations.

The Reynolds stress profiles for M_∞=0.875 at five axial locations are shown in Figure 10. It can be seen in the figure that the calculated and the measured Reynolds stress profiles at x/c=-0.25 compare favorably with each other, which, again, indicates that the inlet boundary condition used in the present study is a good approximation to the experiment at the inlet boundary. At low free stream Mach numbers for which the shock wave -boundary layer interaction do not exist, the flow separation is caused by the turbulent shear stress developing over the forward part of the curved hill [38]. A successful prediction of such a flow depends on the capability of a turbulence model to correctly describe the turbulence field subjected to the streamline curvature [20]. As shown in this figure, the present numerical results compare more favorably with the measured Reynolds stress

24

than the other numerical results at x/c=0.69 and 0.75. However, the magnitude of the present numerical results is slightly smaller than the measured data at these locations. The calculated shocks and separation points are located slightly downstream of the measured data at high free stream Mach numbers, which is attributed to the slightly under-predicted Reynolds stress in the forward part of the curved hill. It is also shown in the figure that the k-ϵ turbulence model with an improved wall function [39] significantly over-estimates the Reynolds stress at x/c=0.75. Inside the reversed flow region, x/c=1.0, the present numerical result compares less favorably with the measured data than does the one obtained using the K-J turbulence model. This under-prediction in the magnitude of the Reynolds stress is attributed to the calculated shock and the separation point which are located slightly downstream of the measured data. It is also shown in the figure that the Reynolds stress profile at x/c=1.38 obtained using a modified K-J turbulence model, with the modifications restricted to the reversed flow region, compares more favorably with the measured data than other numerical results. However, this model is shown to over-predict the Reynolds stress near the outer edge of the reversed flow region.

In the course of the development of the present numerical method, the same transonic flow at M_∞=0.875 has been solved using a k-ϵ turbulence model supplemented with the same near-wall turbulence model as used in the present study. The k-ϵ turbulence model [22] also successfully predicted the existence of the reversed flow region at all free stream Mach numbers. However, the size of the reversed flow region for each free stream Mach number was approximately 10 percent smaller than the present result. The smaller size of the reversed flow region is due to the incapability of k-ϵ

25

turbulence models to resolve turbulence fields in strongly inequilibrium state such as that inside the reversed flow region. The turbulent kinetic energy obtained using the present M-S turbulence model is almost the same as that obtained using the k-ϵ turbulence model. Both turbulence models significantly under-predicted the turbulent kinetic energy, see [22] for more details.

CONCLUSIONS

Calculations of turbulent transonic flows with a control-volume method based on a pressure correction method were presented. The turbulence was described by a multiple-time-scale turbulence model supplemented with a "partially low Reynolds number" near-wall turbulence model.

The numerical results showed that the supersonic pocket on the top of the curved hill first appeared at the free stream Mach number of 0.80 and that the supersonic pocket became larger as the free stream Mach number was further increased. The numerical results also showed that there exists a reversed flow region at low free stream Mach numbers and that the size of the reversed flow region grows extensively as the free stream Mach number is increased. Thus the numerical method was shown to yield a significantly accurate solution for the complex compressible turbulent flow including the supersonic pocket and the nearly incompressible low Mach number reversed flow region.

For turbulent flows over a curved hill, the mean flow is subjected to extra strains caused by the streamline curvature. The development of the turbulence field over such a curved surface mostly depends on the extra strains. The capability to predict the reversed flow region in turbulent flows over a curved hill rests on the capability of a turbulence model to

properly resolve the turbulence field. It was shown that the present

turbulence model can predict the reversed flow region at low free stream

Mach numbers while the Jones-Launder k-ε turbulence model and a k-ε

turbulence model supplemented with a streamline curvature correction method

fail to predict the reversed flow region [5,6]. The present numerical

results also show the extensive growth of the reversed flow region caused

by the shock wave - turbulent boundary layer interaction at high free

stream Mach numbers. These numerical result compare favorably with the

measured data and the other numerical results obtained using the

King-Johnson turbulence model [5].

REFERENCES

1. W. D. Bachalo and D. A. Johnson, "An Investigation of Transonic Turbulent Boundary Layer Separation Generated on an Axisymmetric Flow Model," AIAA Paper 79-1479, 1979.

2. S.-W. Kim, "A Control-Volume Based Reynolds Averaged Navier-Stokes Equation Solver Valid at All Flow Velocities," NASA TM-101488, 1989.

3. S.-W. Kim and C.-P. Chen, "A Multiple-Time-Scale Turbulence model Based on Variable Partitioning of the Turbulent Kinetic Energy Spectrum", Numer. Heat Transfer, Part B, vol. 16, pp. 193-211, 1989. Also available as NASA CR-179222, 1988.

4. S.-W. Kim, "A Near-Wall Turbulence Model and Its Application to Fully Developed Turbulent Channel and Pipe Flows," To appear in Numer. Heat Transfer, 1990. Also available as NASA TM-101399, 1988.

5. D. A. Johnson, "Transonic Separated Flow Prediction with an Eddy-Viscosity/Reynolds-Stress Closure Model," J. AIAA, vol. 25, pp. 252-259, 1987.

6. C. C. Horstman and D. A. Johnson, "Prediction of Transonic Separated Flows," J. AIAA, vol. 22, No. 7, pp. 1001-1003, 1984.

7. D. A. Johnson, C. C. Horstman and W. D. Bachalo, "Comparison Between Experiment and Prediction for a Transonic Turbulent Separated Flow," J. AIAA, vol. 20, pp. 737-744, 1982.

8. S. V. Patankar, Numerical Heat Transfer and Fluid Flow, McGraw-Hill, New York, 1980.

9. A. D. Gosman and F. J. K. Ideriah, "TEACH -T," Department of Mechanical Engineering, Imperial College, London, 1982.

10. R. M. Beam and R. F. Warming, "An Implicit Factored Scheme for the Compressible Navier-Stokes Equations," J. AIAA, vol. 16, pp. 393-402,

1978.

11. R. W. MacCormack, "A Numerical Method for Solving the Equations of Compressible Viscous Flow," _J. AIAA_, vol. 20, pp. 1275-1281, 1982.

12. J. L. Steiger and R. F. Warming, "Flux-Splitting of the Invicid Gasdynamic Equations with Application to Finite Difference Method," _J. Comput. Physics_, vol. 40, pp. 263-293, 1981.

13. S. E. Rogers, D. Kwak, and J. L. C. Chang, "INS3D - An Incompressible Navier-Stokes Code in Generalized Three-Dimensional Coordinates," NASA TM-100012, 1987.

14. C. M. Rhie, "A Pressure Based Navier-Stokes Solver Using the Multi-Grid Method," AIAA 24th Aerospace Sciences Meeting, AIAA-86-0207, 1986.

15. K. C. Karki, and S. V. Patankar, "A Pressure Based Calculation Procedure for Viscous Flows at All Speeds in Arbitrary Configurations," AIAA Paper 88-0058, 1988.

16. Y.-S. Chen, "Viscous Flow Computations Using a Second-Order Upwind Differencing Scheme," AIAA Paper 88-0417, 1988.

17. S. P. Vanka, B. C. J. Chen and W. T. Sha, "A Semi Implicit Calculation Procedure for Flows Described in Boundary Fitted Coordinate System," _Numer. Heat Transfer_, vol. 3, pp. 1-19, 1980.

18. C. R. Maliska and G. D. Raithby, "A Method for Computing Three Dimensional Flows Using Non-Orthogonal Boundary-Fitted Coordinates," _Int. J. Numer. Meth. Fluids_, vol. 4, pp. 519-537, 1984.

19. G. D. Raithby and G. E. Schneider, "Numerical Solution of Problems in Incompressible Fluid Flow: Treatment of the Velocity-Pressure Coupling," _Numer. Heat Transfer_, vol. 2, p. 417, 1979.

20. S.-W. Kim, "Numerical Investigation of an Internal Layer in Turbulent Flow over a Curved Hill," NASA TM-102230, 1989.

21. S.-W. Kim, "Calculation of Reattaching Shear Layers in Divergent Channel with a Multiple-Time-Scale Turbulence Model," AIAA Paper 90-0047, 1990.

22. S.-W. Kim, "Numerical Computation of Shock Wave - Turbulent Boundary Layer Interaction in Transonic Flow over an Axisymmetric Curved Hill," NASA TM-101473, 1989.

23. J. L. Lumley, "Turbulence Modelling," ASME J. Applied Mechanics, vol. 50, pp. 1097-1103, 1983.

24. K. Hanjelic, B. E. Launder, and R. Schiestel, "Multiple-Time-Scale Concepts in Turbulent Shear Flows" in L. J. S. Bradbury, F. Durst, B. E. Launder, F. W. Schmidt, and J. H. Whitelaw, (eds.), Turbulent Shear Flows, vol. 2, pp. 36-49, Springer-Verlag, New York, 1980.

25. Viegas, J. R., Rubesin, M. W., and Horstman, C. C., "On the Use of Wall Functions as Boundary Conditions for Two-Dimensional Separated Compressible Flows," AIAA Paper 85-0180, 1985.

26. J. J. Gorski, "A New Near-Wall Formulation for the k-ϵ Equations of Turbulence," AIAA Paper 86-0556, 1986.

27. R. S. Amano, "Development of a Turbulent Near-Wall Model and Its Application to Separated and Reattached Flows," Numerical Heat Transfer, vol. 7, pp. 59-75, 1984.

28. V. C. Patel, W. Rodi and G. Scheuerer, "Turbulence Models for Near Wall and Low Reynolds Number Flows: A Review", J. AIAA, 23, pp. 1308-1319 (1985).

29. M. Wolfshtein, "The Velocity and Temperature Distribution in One-Dimensional Flow with Turbulence Augmentation and Pressure Gradient," Int. J. Heat and Mass Transfer, vol. 12, pp. 301-318, 1969.

30. F. M. White, Viscous Fluid Flow, McGraw-Hill, New York, 1974.

31. M. J. Zucrow and J. D. Hoffman, Gas Dynamics, vol. 1, John Wiley & Sons, New York, 1976.

32. R. I. Issa, A. D. Gosman, and A. P. Watkins, "The Computation of Compressible and Incompressible Recirculating Flows by a Non-Iterative Implicit Scheme," J. Comput. Physics, vol. 62, pp. 66-82, 1986.

33. F. H. Harlow and P. I. Nakayama, "Transport of Turbulence Energy Decay Rate," Los Alamos Sci. Lab., LA-3854, 1968.

34. V. G. Harris, J. A. H. Graham, and S. Corrsin, "Further Experiments in Nearly Homogeneous Turbulent Shear Flow," J. Fluid Mech., vol. 81, pp. 657-687, 1977.

35. G. Fabris, P. T. Harsha, and R. B. Edelman, "Multiple-Scale Turbulence Modelling of Boundary Layer Flows for Scramjet Applications," NASA CR-3433, 1981.

36. S. J. Kline et. al., Eds., The 1980-1981 AFOSR-HTTM Stanford Conference on Complex Turbulent Flows, vol. 1-3, 1981.

37. P. S. Klebanoff, "Characteristics of Turbulence in a Boundary Layer with Zero Pressure Gradient," NACA Report 1247, 1955.

38. V. Baskaran, A. J. Smits and P. N. Joubert, "A Turbulent Flow over a Curved Hill: Part I. Growth of an Internal Boundary Layer, J. Fluid Mechanics, vol. 182, pp. 47-83, 1987.

39. M. W. Rubesin and J. R. Viegas, "Turbulence Modelling in Transonic Flow," Transonic Symposium - Theory, Application and Experiment, NASA Langley Research Center, Hampton, Virginia, April, 1988.
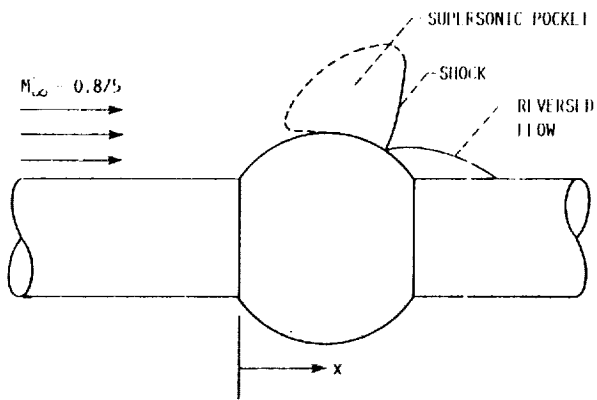
FIGURE 1. - TRANSONIC FLOW OVER AN AXISYMMETRIC CURVED HILL.
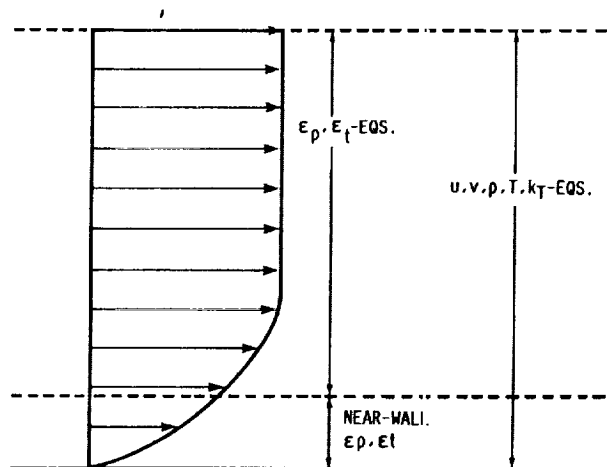
FIGURE 2. - DOMAIN FOR EACH PARTIAL DIFFERENTIAL EQUATION.
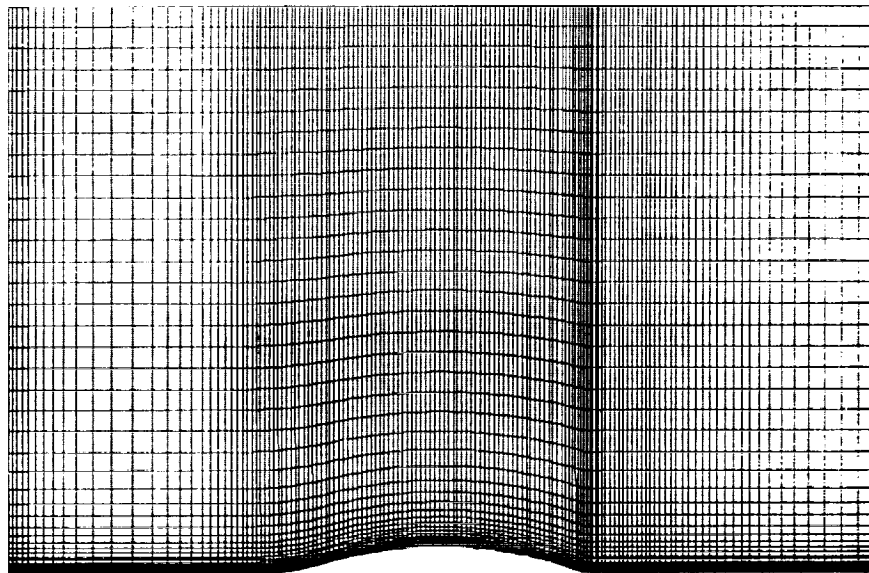
FIGURE 3. - DISCRETIZATION OF THE FLOW DOMAIN (144 x 65 MESH).

(a) RELATIVE ERRORS.

Legend:
△ U VELOCITY
◇ V VELOCITY
○ PRESSURE
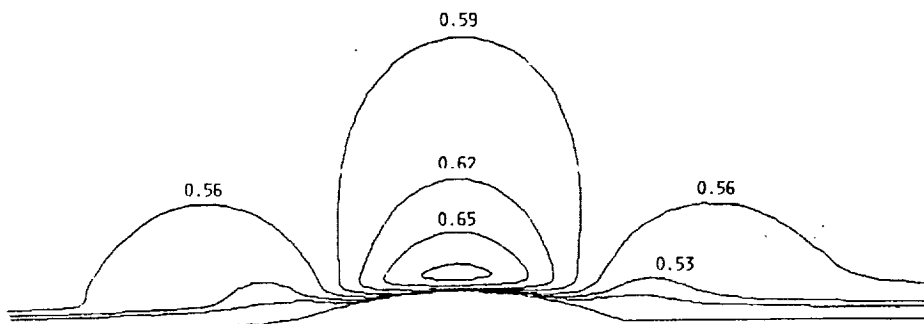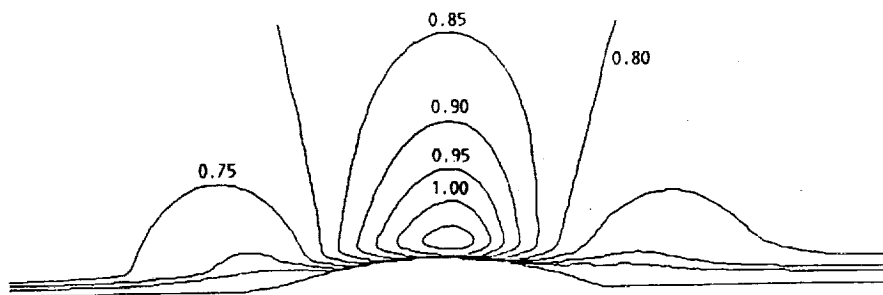□ TEMPERATURE
○ MASS IMBALANCE

E-NORM

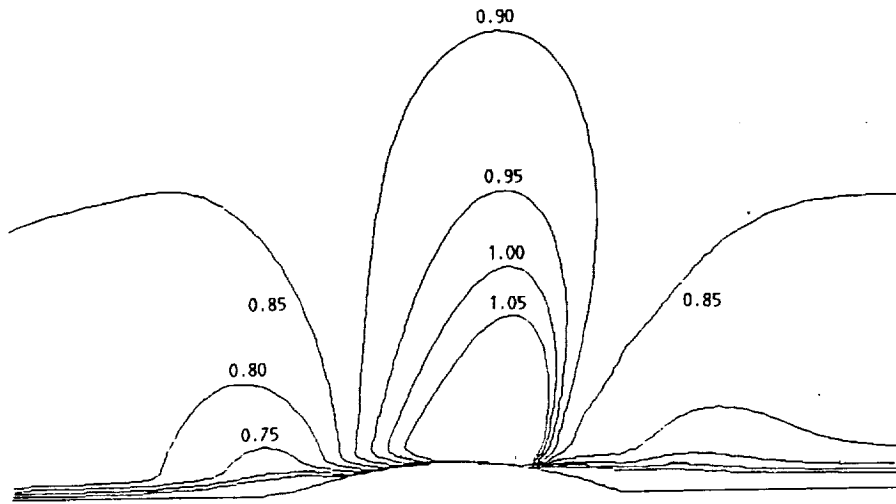(b) MASS IMBALANCE.
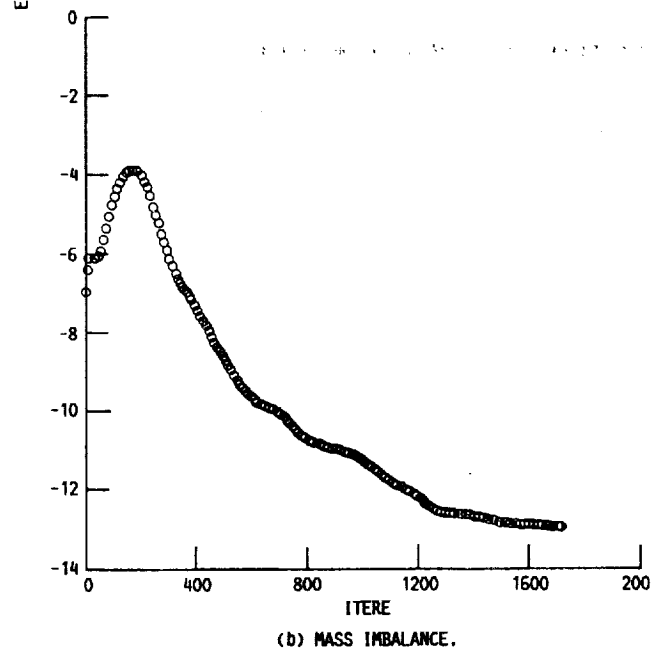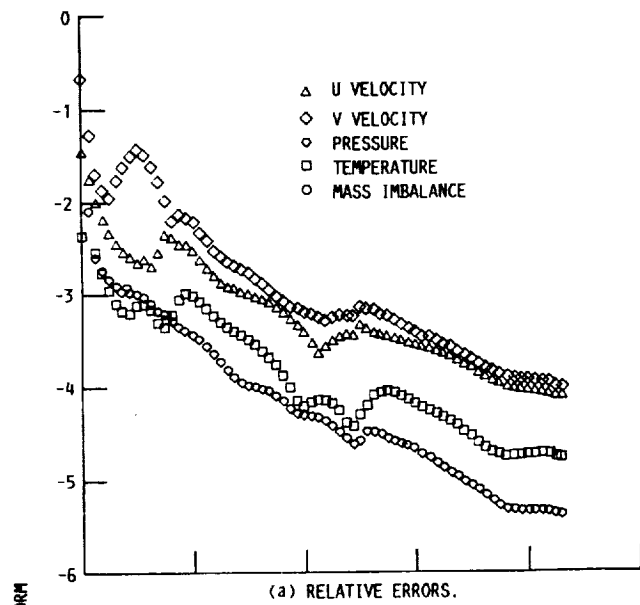
FIGURE 4. - CONVERGENCE HISTORY.

33
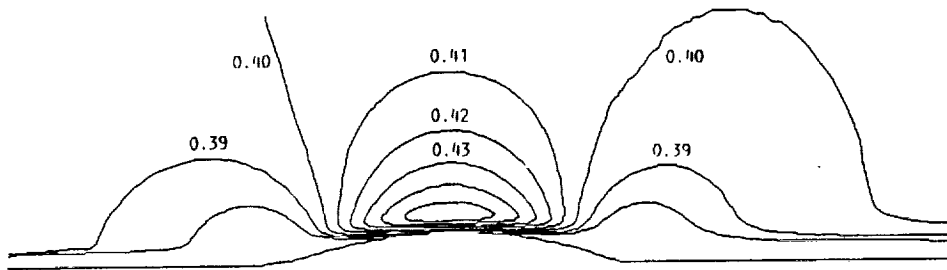
(a) $M_\infty = 0.40$.

(b) $M_\infty = 0.60$.

(c) $M_\infty = 0.80$.

FIGURE 5. - ISO-MACH LINES.

(d) $M_\infty = 0.875$.
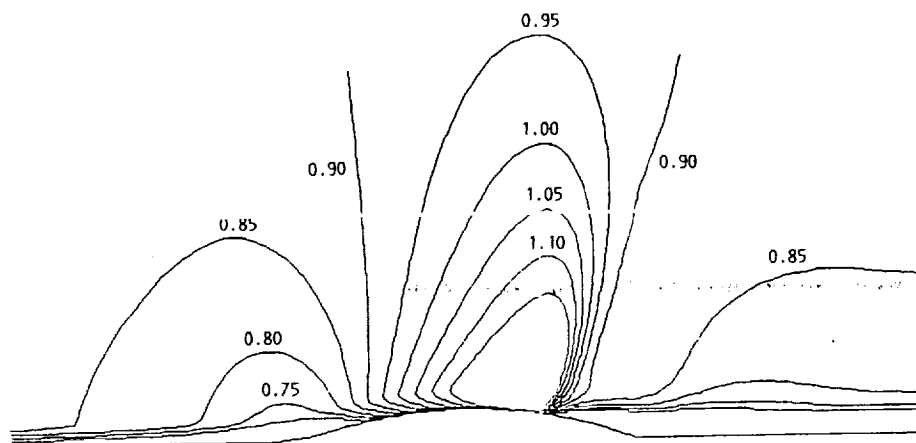
(e) $M_\infty = 0.90$.
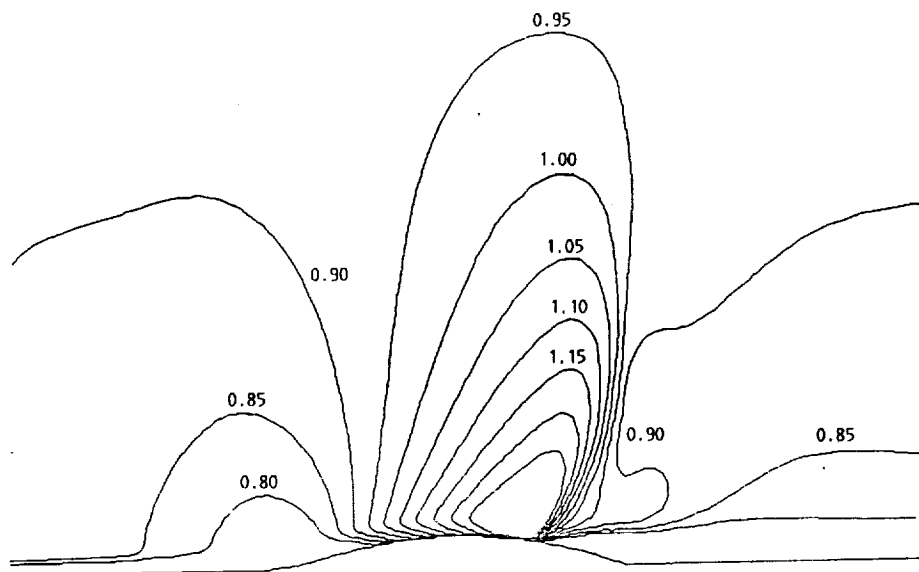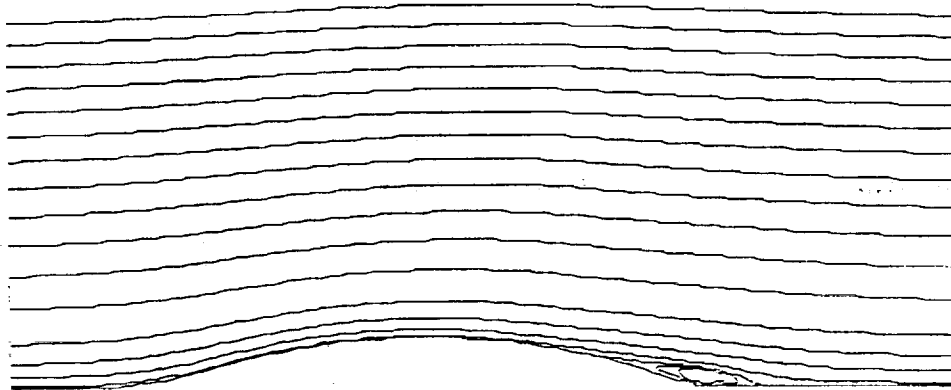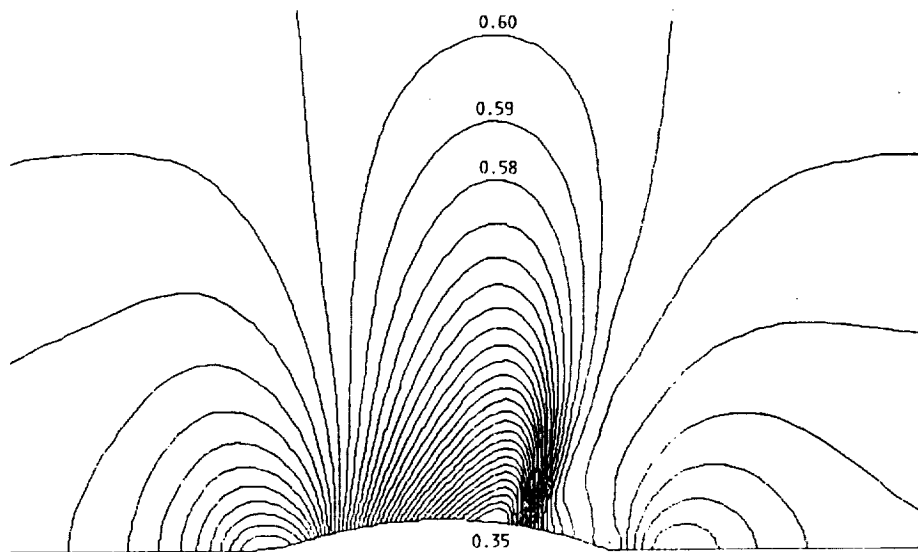

(f) $M_\infty = 0.925$.

FIGURE 5. - CONCLUDED.

35
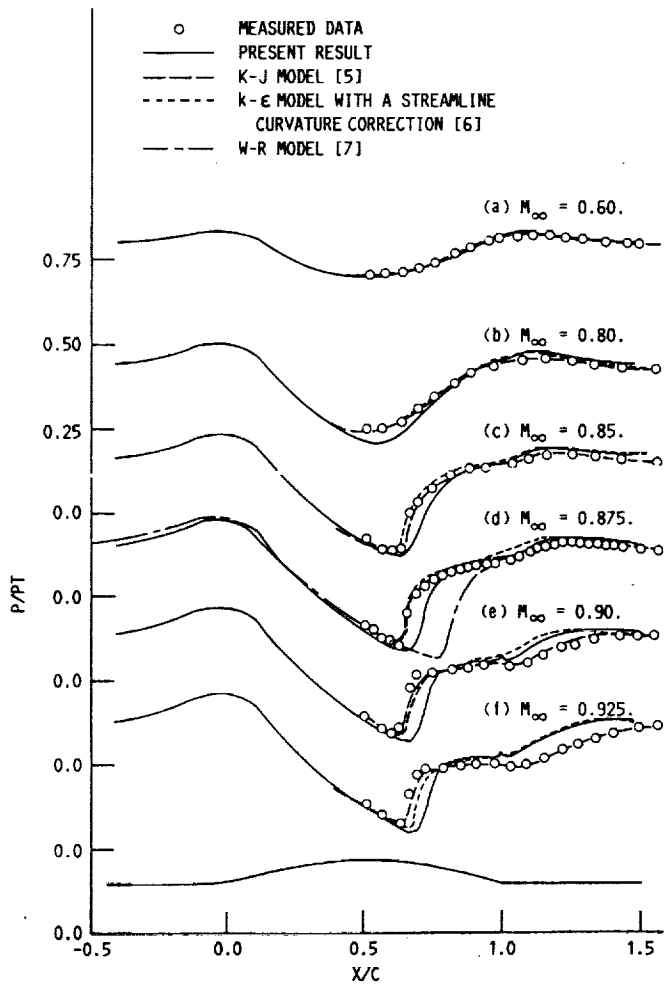
FIGURE 6. - PRESSURE DISTRIBUTION ON THE WALL.

(a) $M_\infty = 0.875$.

(b) $M_\infty = 0.875$.

FIGURE 7. - STREAMLINE AND PRESSURE CONTOURS.

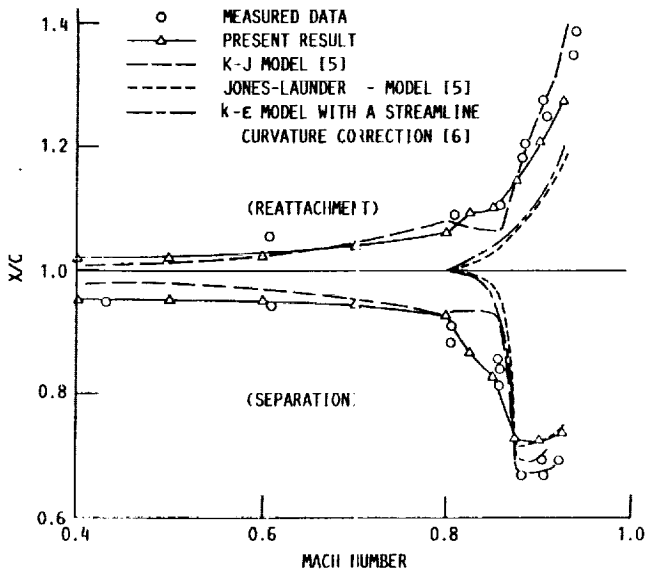37

FIGURE 8. - FLOW SEPARATION AND REATTACHMENT LOCATIONS.
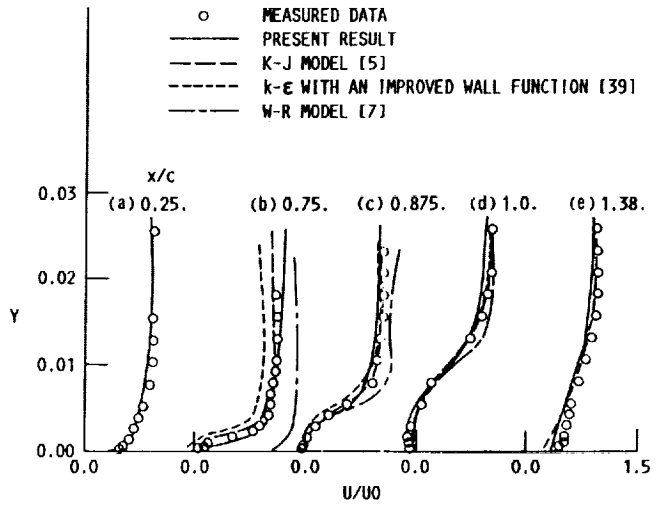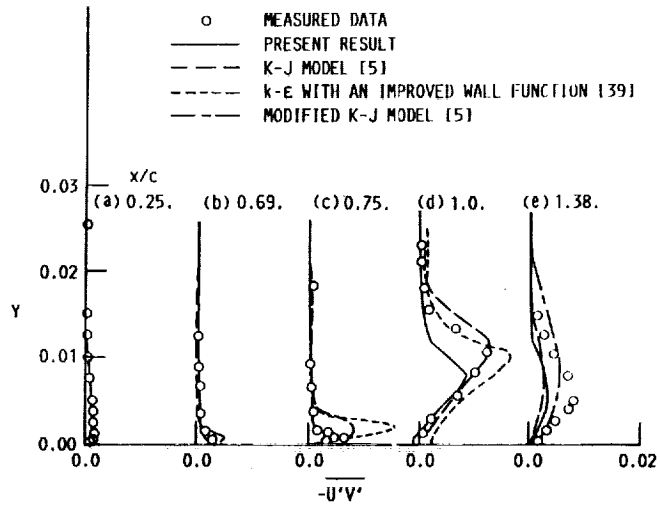

FIGURE 9. - MEAN VELOCITY PROFILES.

FIGURE 10. - REYNOLDS STRESS PROFILES.

38

NASA
National Aeronautics and
Space Administration

Report Documentation Page

1. Report No. NASA TM-102499 ICOMP-90-04	2. Government Accession No.	3. Recipient's Catalog No.
4. Title and Subtitle		5. Report Date
Numerical Investigation of Separated Transonic Turbulent Flows With a Multiple-Time-Scale Turbulence Model		January 1990
		6. Performing Organization Code
7. Author(s)		8. Performing Organization Report No.
S.-W. Kim		E-5295
		10. Work Unit No.
		505-62-21
9. Performing Organization Name and Address		11. Contract or Grant No.
National Aeronautics and Space Administration Lewis Research Center Cleveland, Ohio 44135-3191		
		13. Type of Report and Period Covered
12. Sponsoring Agency Name and Address		Technical Memorandum
National Aeronautics and Space Administration Washington, D.C. 20546-0001		14. Sponsoring Agency Code

15. Supplementary Notes

16. Abstract

Numerical investigation of transonic turbulent flows separated by streamline curvature and shock wave—boundary layer interaction is presented. The free stream Mach numbers considered are 0.4, 0.5, 0.6, 0.7, 0.8, 0.825, 0.85, 0.875, 0.90, and 0.925. In the numerical method, the conservation of mass equation is replaced by a pressure correction equation for compressible flows and thus incremental pressure is solved for instead of density. The turbulence is described by a multiple-time-scale turbulence model supplemented with a near-wall turbulence model. The present numerical results show that there exists a reversed flow region at all free stream Mach numbers considered whereas various k-ε turbulence models fail to predict such a reversed flow region at low free stream Mach numbers. The numerical results also show that the size of the reversed flow region grows extensively due to the shock wave—turbulent boundary layer interaction as the free stream Mach number is increased. These numerical results show that the turbulence model can resolve the turbulence field subjected to extra strains caused by the streamline curvature and the shock wave—turbulent boundary layer interaction and that the numerical method yields a significantly accurate solution for the complex compressible turbulent flow.

17. Key Words (Suggested by Author(s))	18. Distribution Statement
Transonic flow; Streamline curvature; Shock wave—boundary layer interaction; Multiple-time-scale turbulence model; Compressible turbulent flows	Unclassified – Unlimited Subject Category 34

19. Security Classif. (of this report)	20. Security Classif. (of this page)	21. No. of pages	22. Price*
Unclassified	Unclassified	40	A03

NASA FORM 1626 OCT 86   *For sale by the National Technical Information Service, Springfield, Virginia 22161